



Diffusion of Cd vacancy and interstitials of Cd, Cu, Ag, Au and Mo in CdTe: A first principles investigation

J.L. Roehl, S.V. Khare *

Department of Physics and Astronomy, The University of Toledo, Toledo, OH 43606, United States

Received 20 September 2013; received in revised form 5 December 2013; accepted 11 December 2013

Communicated by: Associate Editor Nicola Romeo

Abstract

We present a first principles study of the diffusion profiles of native Cd, adatom and vacancy, and cationic non-native interstitial adatoms Cu, Ag, Au, and Mo in bulk CdTe. The high symmetry Wyckoff position 4(b) is the global minimum energy location for Cd and Ag interstitials and the 4(d) site for Mo interstitials. Adatoms of Cu and Au show an asymmetric shape of the energy diffusion barrier with two structurally equivalent minima and two energetically distinct maxima in the pathway. The others, Mo, Ag and Cd interstitial and vacancy, show a symmetric diffusion barrier with two structurally unique minima and a maximum. Diffusion for Cu and Au interstitials proceeds along the [1 10] channel in the crystal in a near straight line path, avoiding both high symmetry 4(b) and 4(d) sites. Diffusion for Cd and Ag proceeds along two nearly straight line paths along [1 1 1] and [1 1-1]. Diffusion for Mo is along the [1 10] channel however it deviates slightly from the straight line paths along [1 1 1] and [1 1-1] avoiding the 4(b) site. The rate-limiting diffusion barriers range from a low of 0.10 eV for the symmetric diffusion path of a Ag interstitial to a high of 1.83 eV for the symmetric diffusion path of a Cd vacancy. The rate-limiting barriers for the others are 0.27 eV for Au, 0.30 eV for Mo, 0.33 eV for a Cd interstitial and 0.46 eV for Cu. The symmetric or asymmetric nature of the diffusion path as well as the bond length and atomic coordination at the energetic-extrema positions influence the size of the diffusion energy barrier. In addition there exists two electronic signatures in the local density of states: one for the bond breaking in the symmetric diffusion barrier paths and the other in the difference in the energy of occupied states between the global minimum and global maximum energy positions.

© 2013 Elsevier Ltd. All rights reserved.

Keywords: Cadmium telluride; Diffusion; Structural properties; Energetic properties

1. Introduction

Recent advancements in thin film technology have enhanced the commercial viability of solar cells to generate electricity. Among them, cadmium telluride (CdTe) based thin film technology has emerged as a leader in the growing market of thin film solar cell module production. The high photon absorption coefficient and optimal band-gap have made CdTe a natural candidate as an absorber material in thin film solar cells. The relatively high chemical stability

of CdTe compared to the elemental and compound precursors used in its preparation has enabled the emergence of numerous film-fabrication techniques to deposit CdTe (Major et al., 2013; Bonnet, 1992; Clemminck et al., 1992; Ghandhi et al., 1987; Rohatgi, 1992; Compaan et al., 1993; McCandless and Sites, 2011). Recent improvements in these techniques have led to higher cell efficiencies (Green et al., 2013) at lower costs. It is well known that the ability to achieve high cell efficiencies depends on the quality of the CdTe layers and the presence of defects affects overall cell efficiencies by altering their semiconductor properties (Birkmire et al., 1992; Soo et al., 1999). Important classes of defects impeding the achievement of

* Corresponding author. Tel.: +1 419 530 2292.

E-mail address: sanjay.khare@utoledo.edu (S.V. Khare).

optimal cell efficiency are point defects such as interstitials, vacancies and substitutions (Wei and Zhang, 2002; Britt and Ferekides, 1993; Durose et al., 1999). Specifically, these may include native Cd and metal atoms such as Cu, Ag, Mo, and Au depending on the back contacts used. It is well known that Cu plays a number of roles in CdTe. For example, the effect of adding Cu to back contacts dopes the CdTe as p-type and improves the Ohmic contact between the back contact and the p-CdTe. Increased cell efficiency has also been observed due to diffusion of Cu from the back contact into the CdTe absorber layer (Gesert et al., 2007). Additionally, the diffusion of Cu into, and its accumulation at, the CdS layer has been the most suspected cause inhibiting long term device stability (Dobson et al., 2000). For the case of Ag in CdTe, a model has been developed to explain the experimentally observed concentration depth profiles of Ag in CdTe (Wolf et al., 2008). This model, and similar models, as well as Kinetic Monte Carlo calculations used for growth simulation, require information about the diffusivity of the various defects which depend on the diffusion barriers. Therefore, the ability to control the mobility and concentration of these point defects makes it important to understand their mass transport pathways in CdTe. The variety of diffusion mechanisms of Cu and other defects have to be understood clearly before their control can be achieved. Such understanding will include knowledge of the structural, energetic and electronic properties of these native and non-native point defects. The results presented here are intended to provide this information and are complementary to results of experimental observations where activation energies are measured indirectly leading to deduction of diffusion barriers (Dzhafarov et al., 2005; Jones et al., 1992; Lyubomirsky et al., 1997). Revealing these pathways by way of direct experimental measurement in the bulk material is a difficult task by current techniques. Therefore, first principles computational methods are suitable for this type of investigation (Roehl et al., 2012; Roehl et al., 2010; Ma and Wei, 2013). The high requirement of computational resources and complexity of the problem has limited the number of studies on this topic. We have addressed this issue and have begun to fill this gap in the literature by investigating the diffusion of cation type defects of Cd, Cu, Ag, Au and Mo in this manuscript by *ab initio* computational methods.

2. Computational method

All computations employed *ab initio* total energy calculations within the local density approximation to density-functional theory (Hohenberg and Kohn, 1964; Kohn and Sham, 1965) using the Vienna *ab initio* simulation package (Kresse and Hafner, 1993; Kresse and Furthmüller, 1996a; Kresse and Furthmüller, 1996b; Kresse, 1993) (VASP) suit of codes. Core electrons were treated by ultra-soft Vanderbilt type pseudopotentials (Vanderbilt, 1990) as supplied by Kresse and Hafner (1994) using the exchange–correlation energy of Ceperly and Alder, as parameterized

by Perdew and Zunger (1981). The single-particle wave functions were expanded in the plane-wave basis using a 275 eV energy cutoff. Higher plane-wave energy cutoff tests indicated that a numerical convergence better than ± 1 meV was achieved. To obtain the absolute minimum in total energy the lattice constant was varied and fit to a parabolic equation as a function of total energy. The calculated lattice constant and bulk modulus of 6.43 Å and 45.91 GPa is within reasonable agreement with the experimental lattice constant and bulk modulus of 6.46 Å and 42 GPa respectively (Madelung, 2004). The CdTe bulk structure consists of a two atom primitive cell zinc-blende structure (space group F-43m number 216) with the Cd and Te atoms at Wyckoff positions 4(a) and 4(c) respectively. A cubic unit cell of this zinc-blende structure consists of 8 atoms. Diffusion barrier calculations were computed in a $3 \times 3 \times 3$ repetition of the cubic unit cell in a 216 atom supercell. Long-range interactions between defects in neighboring supercells are reduced using the larger supercell size which more closely models an isolated defect. A Gamma point Monkhorst–Pack (Monkhorst and Pack, 1976) generated *k*-point grid was used for the Brillouin-zone integrations in all calculations. Larger *k*-point sampling tests indicated that a numerical convergence better than ± 3 meV was achieved. The minimum energy for each configuration was found by allowing all atoms to fully relax. Relaxation was considered complete when a force tolerance of 0.01 eV/Å was reached for each atom. The local density of states (LDOS) calculations were performed with the Gaussian smearing scheme. The nudged elastic band (NEB) method Mills and Jónsson, 1994 was used for the diffusion barrier calculations.

3. Results and discussion

3.1. Interstitial diffusion

The simplest mode of diffusion in zinc-blende CdTe is interstitial diffusion down the spacious [110] channel. Interstitial diffusion down this channel consists of the diffusing adatom passing between two alternating high symmetry sites, Wyckoff positions 4(b) and 4(d). The 4(b) site is the location of the diffusing adatom when it is tetrahedrally coordinated by Te atoms, thus labeled T_{Te} , and the 4(d) site is the location of the diffusing adatom when it is tetrahedrally coordinated by Cd atoms, thus labeled T_{Cd} . The global minimum energy site (GME) for an interstitial of Cd and Ag were found to be at the T_{Te} site and for Mo it was at T_{Cd} . The GME was found to be off the high symmetry site for interstitials of Cu and Au. For vacancy diffusion the GME was found where the bulk Cd atom was removed from its bulk 4(a) site and the surrounding atoms were allowed to relax until convergence. Using these GME sites, as the initial and final positions, NEB runs were performed for finding the diffusion energy barriers. An odd number of images were used for symmetric barriers

and a distance of 0.5 Å was maintained between images to confirm diffusion barriers.

3.2. Structural properties

As the interstitial adatom diffuses down the [110] channel we see that different species occupy different extrema positions and atomic configurations. As Cd, Ag and Mo interstitials diffuse between adjacent unit cells down the [110] channel they encounter a GME, a secondary minimum energy position (SME) and a global maximum energy position (GMax). While Cu and Au interstitials diffuse between adjacent unit cells they also encounter a GME and a GMax. However, unlike Cd, Ag and Mo, diffusion paths for Cu and Au interstitial possess a secondary maximum energy position (SMax) and do not possess a SME. These different extrema positions and atomic configurations are shown in Fig. 1. This figure shows an example of three different bonding scenarios; the first in Fig. 1 panels (a–c), the second in panels (d–f) and the third in panels

(g–i). The first scenario involves both 4(b) and 4(d) sites as SME and GME respectively and the sp^2 like Cd and Te coordinated site as the GMax, for Cd. The second bonding scenario, for Ag, where both 4(b) and 4(d) sites reverse roles as the GME and SME respectively. The third one involves neither of the high symmetry sites but includes the sp^2 like Cd and Te coordinated site as the GME, for Cu and Au, where only Cu is shown. The extrema positions for the Cd, Cu, Au, Ag and Mo interstitials are given in Table 1. For the configurations in Fig. 1, averages for both, bond lengths and angles, are given in Table 2 and the diffusion barriers for all diffusing species are given in Table 3. The broken symmetry of the Ag GMax position makes interpreting average bond lengths and angles for this position ambiguous and therefore these are omitted in Table 2.

3.2.1. Cd

The Cd interstitial GME position, Fig. 1(a), occupies the T_{Te} tetrahedrally coordinated position making an average angle of 109.5° with its nearest neighbor Te atoms. The

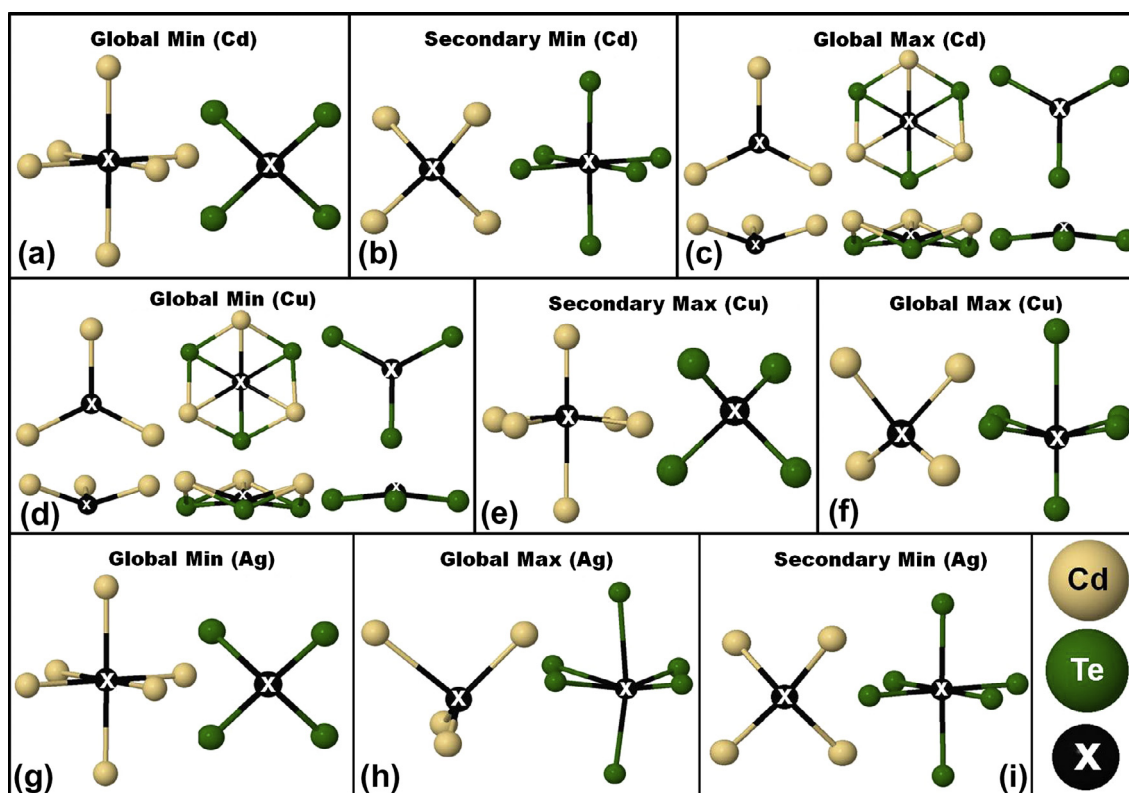


Fig. 1. Structural properties and bonding configuration of interstitial positions corresponding to various minimum and maximum energy sites. The atom labeled x is the diffusing interstitial atom; the surrounding atoms are Cd (light yellow) and Te (dark green). The Cd interstitial global minimum energy (GME) position (a) occupies a tetrahedrally coordinated position with neighboring Te atoms and an octahedral site with neighboring Cd atoms. The Cd secondary minimum energy (SME) position (b) reverses the coordination observed for the GME (a). The Cd global maximum (GMax) position (c), located between the GME and SME position, forms an sp^2 like configuration with both neighboring Cd and Te atoms. Individual Cd and Te sp^2 like bonding is also shown in panel (c) for clarity. The Cu interstitial extrema positions are similar to those of Cd but occur at different configurations. The Cu interstitial GME (d) occurs at a sp^2 like configuration, similar to the GMax for Cd (c). The Cu secondary maximum (SMax) configuration is shown in (e) and the GMax configuration is shown in (f). The Ag interstitial GME (g) occupies a tetrahedrally coordinated position with neighboring Te atoms and an octahedral site with neighboring Cd atoms. The Ag SME (i) reverses the coordination observed for the GME (g). The Ag GMax (h) occurs on either side of the SME (i) where the symmetry of the SME position is broken. (For interpretation of the references to colour in this figure legend, the reader is referred to the web version of this article.)

Table 1

Extrema positions given in direct coordinates, $\mathbf{R} = c_1\mathbf{a}_1 + c_2\mathbf{a}_2 + c_3\mathbf{a}_3$, of a fcc unit cell $\mathbf{a}_1 = a[0, 0.5, 0.5]$, $\mathbf{a}_2 = a[0.5, 0, 0.5]$, $\mathbf{a}_3 = a[0.5, 0.5, 0]$. For example the Mo secondary minimum position is given by $\mathbf{R}[\text{Mo}] = 0.53\mathbf{a}_1 + 0.53\mathbf{a}_2 + 1.48\mathbf{a}_3$.

Element	Global min			Secondary min			Secondary max			Global max		
	c_1	c_2	c_3	c_1	c_2	c_3	c_1	c_2	c_3	c_1	c_2	c_3
Cd	0.50	0.50	0.50	0.75	0.75	0.75				0.65	0.65	0.66
	0.50	0.50	1.50									
Cu	0.60	0.60	0.60				0.54	0.54	1.46	0.66	0.66	0.83
	0.60	0.60	1.60									
Ag	0.50	0.50	0.50	0.75	0.75	0.75				0.69	0.69	0.69
	0.50	0.50	1.50									
Au	0.61	0.61	0.61				0.57	0.57	1.35	0.70	0.70	0.80
	0.61	0.61	1.61									
Mo	0.75	0.75	0.75	0.53	0.53	1.48				0.62	0.62	1.14
	0.75	0.75	1.75									

Table 2

Average bond length and angle from interstitial defect to the first two shells of neighbors which are either only Te atoms or only Cd atoms.

Element	Position	Fig. 1	Nearest-neighbor	Avg. bond length (Å)	Avg. bond angle (°)
Cd	Global min	A	Te	3.25	90.0
			Cd	2.93	109.5
	Secondary min	B	Te	2.85	109.5
			Cd	3.33	90.0
	Global max	C	Te	2.83	114.1
			Cd	2.89	119.0
Cu	Global min	C	Te	2.61	119.1
			Cd	2.82	112.8
	Secondary max	B	Te	2.74	109.2
			Cd	3.30	89.7
	Global max	A	Te	3.23	88.1
			Cd	2.92	107.9
Ag	Global min	D	Te	2.86	109.5
			Cd	3.26	90.0
	Secondary min	F	Te	3.20	90.0
			Cd	2.91	109.5
	Global max	E	Te	–	–
			Cd	–	–

Cd GME also occupies a sp^3d^2 octahedral site with the closest Cd atoms making an average angle of 90° . The Cd SME, Fig. 1(b), reverses the coordination observed for the GME in (a) occupying the bulk like T_{Cd} position with nearest neighbor Cd atoms and an octahedral site with the closest Te atoms making identical angle of 109.5° and 90.0° respectively. The Cd SME bonding is comparable to the bulk Cd bonding with a slight increase of Cd–Te and Cd–Cd bond length of 2.52% and 3.60% respectively

Table 3

Diffusion barriers (eV) for different point defects. The columns marked secondary min (max) have values entered only when a secondary minimum (maximum) energy site exists.

Element	Secondary min (eV)	Secondary max (eV)	Global max (eV)
Cd ^v	–	–	1.83
Cd ^l	0.04	–	0.33
Cu	–	0.12 (0.12 ^a)	0.46 (0.43 ^a , 0.33 ^b , 0.57 ^c)
Ag	0.08 (0.06 ^a)	–	0.10 (0.08 ^a , 0.15 ^d)
Au	–	0.12	0.27
Mo	0.02	–	0.30

^a Theoretical values from Ma and Wei (2013).

^b Experimental value from Dzhanfarov et al. (2005).

^c Experimental value from Jones et al. (1992).

^d Experimental value from Lyubomirsky et al. (1997).

which explains the small difference in energy of 0.04 eV between the SME and the GME. The Cd GMax, Fig. 1(c) located between the GME and SME, forms an sp^2 like configuration with both nearest neighbor Cd and Te atoms. We see that the Cd interstitial in Fig. 1(c) forms more of a planer sp^2 like bond with its three neighboring Cd bulk atoms at distance of 2.89 Å making a Cd–Cd–Cd angle of 119° with the Cd interstitial, close to the ideal sp^2 angle of 120° . The three neighboring Te atoms are 2.83 Å away and make a Te–Cd–Te angle of 114.1° with the Cd interstitial indicating that the Cd interstitial has moved further away from the center of the Te sp^2 plane than for the Cd sp^2 plane. Individual Cd and Te sp^2 like bonding is also shown in panel (c) for clarity. We see this bonding configuration in a number of extrema positions for the other interstitials. This sp^2 like configuration is the GME position for a Cu and Au interstitial and it serves as the GMax for a Mo interstitial.

3.2.2. Cu

As mentioned in Section 3.2.1, the Cu interstitial GME position forms a nearly planer sp^2 like bond with its

neighboring Te bulk atoms, Fig. 1(d), with an angle 119.1° , close to the ideal sp^2 angle of 120° , at a distance of 2.61 \AA . The Cu interstitial bonding with the neighboring Cd bulk atoms is less planar with a Cd–Cu–Cd bond angle of 112.8° at a distance of 2.82 \AA . We see that the Cu interstitial SMax and GMax, Fig. 1(e and f) respectively, deviate from the high symmetry 4(b) and 4(d) sites. At the SMax, Fig. 1(e), the Cu interstitial forms a slightly distorted T_{Te} position with a Te–Cu–Te bond angle of 109.2° and a distorted octahedral coordination with the neighboring Cd atoms with a less than ideal Cd–Cu–Cd bond angle of 89.7° . At the Cu interstitial GMax, Fig. 1(f), the coordination reverses and the distortion is more pronounced. The Cu interstitial GMax is a distorted T_{Cd} position with a Cd–Cu–Cd bond angle of 107.9° and a distorted octahedral coordination with the neighboring Te atoms with a Te–Cu–Te bond angle of 88.1° . As the Cu interstitial moves from the GME to the GMax the Cu–Cd bond length only increases 3.55% from 2.82 \AA to 2.92 \AA but the Cu–Te bond length changes significantly by 23.8% increasing from 2.61 \AA to 3.23 \AA . Comparing this to the situation for a Cd interstitial where the Cd–Cd bond length decreases 1.37% from 2.93 \AA to 2.89 \AA and the Cd–Te bond length decreases 12.9% from 3.25 \AA to 2.83 \AA , much less than the Cu–Te bond length change, may explain in part why the Cu Gmax energy barrier of 0.46 eV is larger than the 0.33 eV GMax energy barrier for a Cd interstitial. The values for the SMax and GMax of 0.12 eV and 0.46 eV , respectively, are in excellent agreement with the theoretical values of 0.12 eV and 0.43 eV reported by Ma and Wei (2013). The rate limiting barrier of 0.46 eV for Cu is also in excellent agreement with the experimental values of 0.33 eV and 0.57 eV reported by Dzhafarov et al. (2005); Jones et al. (1992) respectively.

3.2.3. Ag

Unlike the Cu interstitial that avoids the high symmetry positions, the Ag interstitial GME, shown in Fig. 1(g), occupies the T_{Te} position making the ideal 109.5° angle with its neighboring Te atoms and an octahedral position making the ideal 90.0° angle with its neighboring Cd bulk atoms. Fig. 1(i) shows the SME where the coordination reverses but the ideal symmetries remain, the Ag interstitial occupies the T_{Cd} position making the ideal 109.5° angle with its neighboring Cd atoms and an octahedral position making the ideal 90.0° angle with its neighboring Te atoms. The SME is only 0.02 eV less than the 0.10 eV GMax energy barrier. The Ag GMax, Fig. 1(h), lies on either side of the SME where the high symmetry of the T_{Cd} position is broken. The broken symmetry of the GMax prevents interpreting average bond lengths and angles for this position. However, we note as the Ag interstitial moves from the GME position to the shallow SME we see the Ag–Cd bond length decreases 10.7% from 3.26 \AA to 2.91 \AA but the strain of this decrease is compensated by an increase in the Ag–Te bond length by 11.9% from 2.86 \AA to 3.20 \AA . This balancing of bulk strain results in the small 0.08 eV difference in

energy between the GME and the SME and may explain the small barrier energy of 0.10 eV at the nearby GMax. The values for the SME and GMax of 0.08 eV and 0.10 eV , respectively, are in excellent agreement with the theoretical values of 0.06 eV and 0.08 eV reported by Ma and Wei (2013). The rate limiting barrier of 0.10 eV for Ag agrees well with the experimental value of 0.15 eV reported by Dzhafarov et al. (2005).

3.3. Diffusion path

3.3.1. Path symmetry

The GME for Cd and Ag interstitials is located at the highly symmetric 4(b) site with the SME occurring at the other complementary high symmetry 4(d) site and the GMax located between the two sites on either side of the 4(d) site. A similar situation occurs for Mo. However, the GME for Mo is located at the 4(d) site with the SME occurring at a slightly distorted 4(b) site and the GMax located between the two sites, immediately on either side of the 4(b) site. In each of these cases, Cd, Ag and Mo, this leads to a symmetric diffusion path down the $[110]$ channel. However, for Cu and Au interstitials, the GME is not located at either of the 4(b) or 4(d) sites but rather at the sp^2 like position and as a result their diffusion paths are asymmetric. Furthermore, Cu and Au diffusion paths do not possess a SME; instead they possess an SMax and an additional GME. The first and second GME, used for the NEB runs, are related by a lattice vector and hence are equivalent sites, the additional GME is not related to the first or second by a lattice vector and as such Cu and Au possess two distinct GME where as Cd, Ag and Mo possess only one distinct GME. This is because the GME for Cu and Au do not occur at either of the 4(d) or 4(b) sites and symmetry of the zinc-blende structure along the $[110]$ channel requires this additional GME position. The additional GMEs for Cu and Au, as well as the different symmetries of all diffusion paths, are clearly seen in Fig. 2.

3.3.2. Path linearity

As noted earlier both Cd and Ag diffusion path minima occur at the 4(b) and 4(d) sites. As a result the diffusion path passes directly between the two alternating 4(b) and 4(d) sites resulting in a diffusion path down the $[110]$ channel that involves alternating linear paths down along the $[1\bar{1}\bar{1}]$ direction, then back up. This saw tooth diffusion behavior of Cd and Ag is shown in Fig. 3(c) for Cd. In contrast, the Cu and Au GME position occurs between the 4(b) and 4(d) sites and the GMax and SMax avoid the 4(d) and 4(b) position resulting in a more linear path down the $[110]$ channel, shown for Cu in Fig. 3(a). The different maxima and minima positions for the different interstitials impacts the z -axis deviation of their respective diffusion paths down the $[110]$ channel. The z -axis deviation in linearity is shown for all interstitials in Fig. 4. Fig. 4 quantitatively shows the linearity of the diffusion path along the $[110]$ channel. The ordinate refers to the change in the

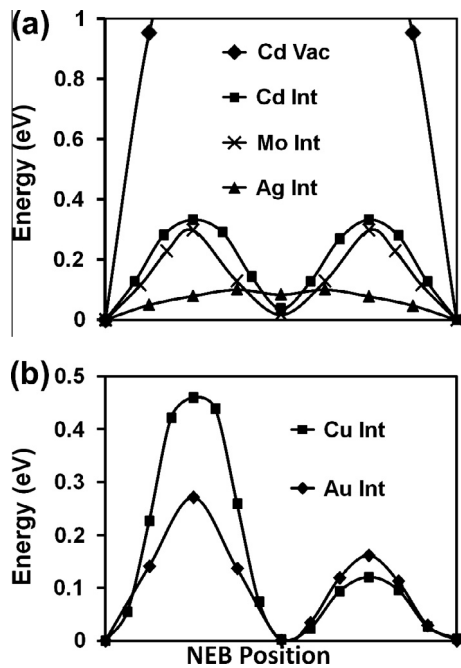


Fig. 2. NEB graphs of diffusion barrier profiles as a function of the NEB step positions, (a) the symmetric barriers (i.e. Cd, Mo and Ag) and (b) the asymmetric barriers of Cu and Au observed in CdTe. The first and last NEB positions on the X -axis are displaced through a lattice vector $a[0.50.50]$ down the $[110]$ channel, where a is the computed lattice constant 6.43 \AA , and hence have identical energies. The symmetric Cd vacancy barrier occurs in the middle of the path with an energy of 1.83 eV .

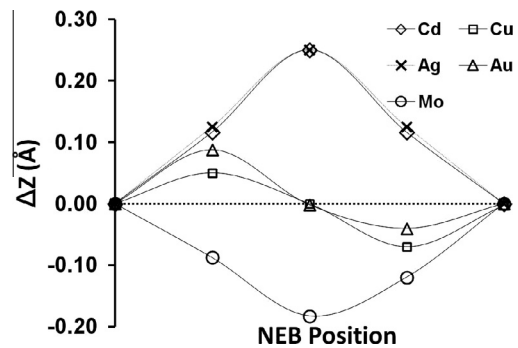


Fig. 4. Z -axis deviation from the minimum of the interstitial atoms while diffusing between global minimums in adjacent unit cells down the $[110]$ channel. The ordinate axis is defined to be zero at the Z -axis position of the diffusing atom in its global minimum energy site.

coordinates, followed by Mo that deviates around 0.20 \AA from the Mo GME. This is expected as the Cd and Ag interstitials travel in the saw tooth pattern between the 4(b) and 4(d) sites. The asymmetric Cu and Au interstitials experience the least deviation from the z -axis coordinate of their GME. We see the linear diffusion character of Cu interstitial deviates approximately 0.05 \AA from the Cu GME z -axis coordinate at both the Gmax and SMax, traveling in an almost straight line path down the $[110]$ channel. The Au interstitial deviates less than 0.10 \AA from its GME when passing through the GMax position but only deviates approximately 0.05 \AA when passing through its SMax.

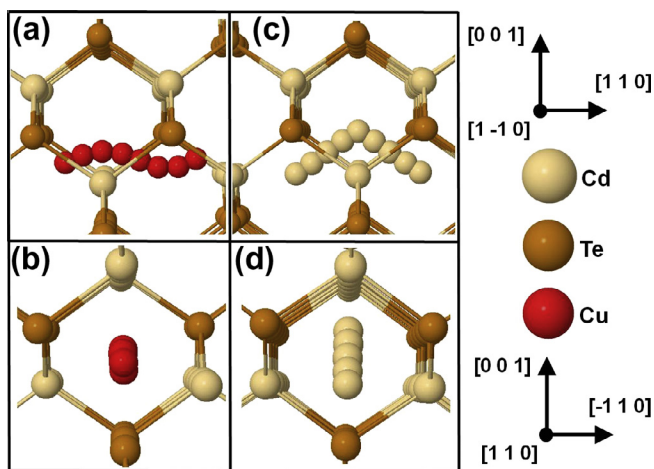


Fig. 3. Differences in diffusing paths for (a), (b) Cu and (c), (d) Cd interstitial atoms down the $[110]$ channel in CdTe. Au atoms have paths similar to Cu while Ag has a path similar to Cd. Mo is similar to Cu and Au, with the global minimum occurring at a high symmetry, 4(d), site. However, the path deviates slightly, avoiding the other high symmetry, 4(b), site where as Cu and Au pass between both high symmetry sites.

3.3.3. Path strain energy

To further explore the relative importance of this z -axis deviation during the diffusion path we focused attention on the symmetric diffusing Cd and asymmetric diffusing Cu interstitials which show the highest and lowest z -axis deviation in Fig. 4.

We performed two additional sets of runs each for a Cd and Cu interstitial to assess the effect of z -axis deviation on local strain energy and relaxation during diffusion. In both sets the interstitial was kept fixed with its x and y coordinates obtained from the images of the fully converged NEB run and all other atoms in the supercell were fixed (i.e. unrelaxed) at their bulk equilibrium positions. For the “straight line” set of runs the z -coordinate of the interstitial was fixed in the entire set at the z -coordinate of the GME. In the “bulk” set the z -coordinate of the interstitial was varied. It was chosen to be the z -coordinate of the corresponding image in the fully converged NEB run. For a Cu interstitial, in Fig. 5(a), we see that the maximum strain energy occurs at the GMax. This can be explained by the distortion of the symmetric T_{Cd} position. This maximum strain energy occurs at the GMax for both the “straight line” and “bulk” energy runs. As the Cu interstitial moves towards the SMax at the T_{Te} position we again see an increase in the “straight line” and “bulk” energy. This can be explained again by the distortion of the symmetric

z -axis, from the minimum energy position z -axis coordinate, at each NEB position (abscissa). As we see from Fig. 4, the largest deviation in the z -axis is for the symmetric diffusing interstitials Cd and Ag, deviating approximately 0.25 \AA from their respective GME z -axis

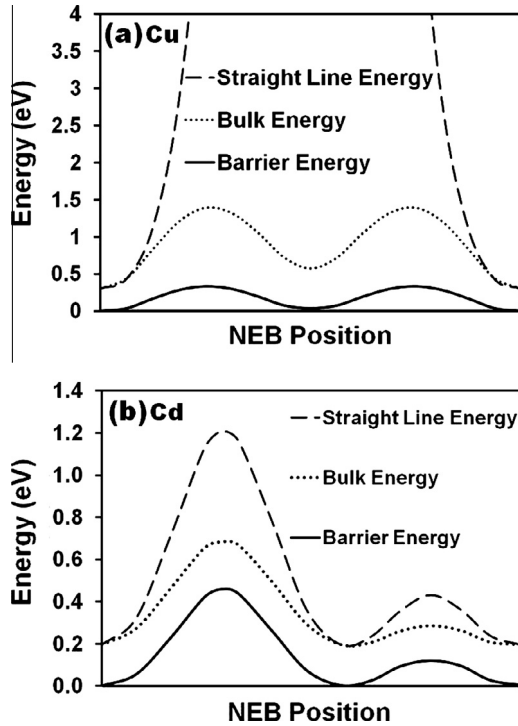


Fig. 5. Effect of local strain energy and relaxation around diffusing interstitial Cu (a) and Cd (b) atoms. The barrier energy represents the fully relaxed diffusion barrier energy as a function of the NEB position along the diffusing path; the bulk energy is the energy of the interstitial located at the relaxed NEB position in an un-relaxed bulk cell, i.e. the remaining atoms are left unrelaxed in their bulk positions; the straight line energy is the energy of the NEB positions located at the same z -axis position as the global minimum energy position in an un-relaxed bulk cell, for Cd (b) the straight line maximum occurs in the middle of the path with an energy of 21.3 eV.

T_{Te} tetrahedral and octahedral bonding configurations. At the GME, the Cu interstitial experiences the least “bulk” and “straight line” energy of around 1.2 eV. For the Cd

interstitial the situation is different, the maximum strain energy occurs at the SME T_{Cd} position. We also note that there is a substantial difference between the “bulk” and “straight line” energies at the maximum strain position for the Cd interstitial, over 20 eV, compared to the difference for the Cu interstitial case where the difference is around 0.6 eV. This can again be explained by the character of the diffusion path. For Cd, the diffusion path is a see-saw pattern that experiences the largest z -axis deviation and hence largest deviation from the straight line path.

3.4. Electronic properties

We computed the electronic local density of states (LDOS) of a variety of configurations of all diffusing species studied. We highlight a few observations from these computations here. An example of a symmetric diffusion barrier is illustrated in Fig. 6. It shows the LDOS for the diffusion of a Ag interstitial as it moves from the GME at the T_{Te} site to the SME at the T_{Cd} position. The Ag interstitial at the GME position, the grey atom marked ‘A’ in Fig. 6(a), is tetrahedrally coordinated to the black Te atoms and octahedrally coordinated to the white Cd atoms. At the SME position, marked ‘B’ in Fig. 6(a), the coordination is reversed. At the GME ‘A’ position the Ag interstitial forms symmetric bonds with Cd atoms 1, 2 and 3 and Te atoms 4, 5 and 6. As the Ag interstitial moves from the GME ‘A’ position to the SME ‘B’ position we see that the three bonds with Cd atoms 1, 2 and 3 and Te atoms 4, 5 and 6 remain intact. Panels (b and c) in Fig. 6 shows the LDOS for the d orbitals of the Ag interstitial, the s orbitals for Cd atoms 1, 2 and 3 and the p orbitals for Te atoms 4, 5 and 6 at (b) the GME and at (c) the SME. At the GME (b) we see two significant s–p bonding peaks from the tetrahedrally coordinated nearest neighbor Cd and Te bulk atoms around -5.13 eV and -5.6 eV and

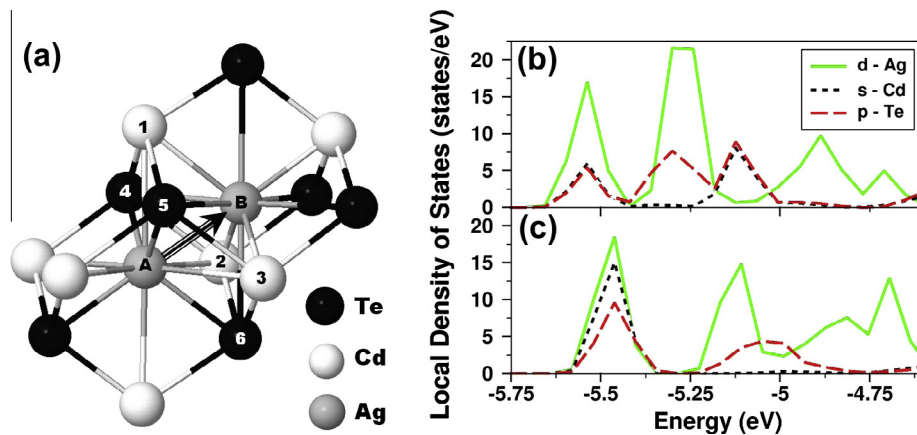


Fig. 6. Panel (a) shows the global minimum energy position marked ‘A’ and secondary minimum energy position marked ‘B’ for an Ag interstitial. Filled black (white) circles show nearest neighbor Te (Cd) atoms. Position A is tetrahedrally coordinated to Te and octahedrally coordinated to Cd. At position B the coordination is reversed. Panels (b and c) show the LDOS of the d orbitals of the Ag interstitial and the p orbitals of nearest neighbor Te atoms 1, 2 and 3 and s orbitals of its nearest neighbor Cd atoms 4, 5 and 6. LDOS for the Ag atom in position ‘A’ is in panel (b), for position ‘B’ in panel (c). At position B, the Ag interstitial d orbitals are shifted toward the Fermi energy, away from the deep binding at position A. However, this shift is accompanied by a shift away from the Fermi, to tighter binding energies for the s and p orbitals of the nearest neighbor Cd and Te atoms respectively. This compensating shift in orbitals may in part explain the low diffusion barrier for Ag interstitials.

two large contributions from the d states of the Ag interstitial again at around -5.13 eV and at -5.25 eV. As the Ag interstitial moves to the SME, in panel (c), we see that the contributions from the Ag p states are shifted to higher energies towards the Fermi level. This is not surprising since the SME is at a less energetically favorable position than the GME. However, this shift in the Ag p states toward higher energies is accompanied by a considerable shift toward deeper binding energies for the s–p bonding peaks of the nearest neighbor Cd and Te atoms. This compensating shift in the LDOS may in part explain the small 0.08 eV difference in energies between the Ag interstitial GME and SME positions as well as the small 0.10 eV energy barrier at the GMax position that occurs between the two as the Ag interstitial moves from GME ‘A’ position to the SME ‘B’ position.

An example of an asymmetric diffusion barrier is illustrated in Fig. 7. It shows the LDOS for an interstitial Cu atom at the GME and GMax positions. We observe in Fig. 7(a) a shift in the d-states of the Cu interstitial to tighter binding energies for the sp^2 like GME compared to that of the distorted T_{Cd} GMax position. In addition we note the three distinct peaks for the GME, at -3.75 eV, -3.25 and around 2.7 eV, can be attributed to the Cu d-state and Te p-state bonding formed with the three neighboring

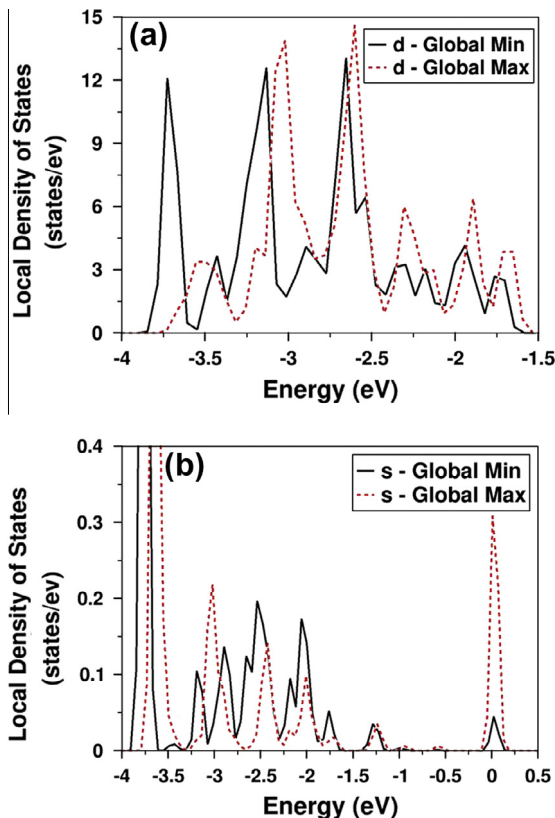


Fig. 7. LDOS for a Cu interstitial at the global minimum and global maximum positions. We observe in (a), the shift in the d-states to tighter binding energies for the global minimum position compared to that of the global maximum. This trend is also observed in (b) the s-states. We also observe a significant increase of the defect like s-states at the Fermi energy for the global maximum compared to the global minimum.

Te atoms in the sp^2 like bonding configuration. The shift toward deeper binding energies for the GME d-states is also observed in the hybridized s-states, as shown in Fig. 7(b). In addition to the shift toward shallow binding energies for the GMax states, we also observe a significant increase of the metallic like s-states at the Fermi energy for the GMax compared to the GME.

4. Conclusion

In this study we have presented an *ab initio* investigation of the bulk diffusion profiles of native Cd, adatom and vacancy, and cationic non-native interstitial adatoms Cu, Ag, Ag and Mo in CdTe. Diffusion profiles for Cd, vacancy and interstitial, Ag and Mo show symmetric pathways while those for Cu and Au appear asymmetric. The results of this study indicate that the rate-limiting diffusion barriers range from a low of 0.10 eV for the symmetric diffusion path of an Ag interstitial to a high of 1.83 eV for the symmetric diffusion path of a Cd vacancy. We have examined the structural interaction associated with the diffusing atom, or vacancy, and the bulk host atoms throughout the diffusion process to further reveal the nuances of the diffusion process. This included investigation of the curvature of the diffusion path, relevant bond angles and lengths, first and second shell coordination, and local density of states. We discovered that bond length and atomic coordination at the energetic-extrema positions in addition to the symmetric or asymmetric nature of the diffusion path can influence the size of the diffusion activation energy. Furthermore, we have found a compensating shift in the LDOS that may explain the small 0.08 eV difference in energies between the Ag interstitial GME and SME positions and the small 0.10 eV energy barrier at the GMax position. In addition to the compensating shift, we have found an electronic signature in the difference in hybridization between the GME and GMax positions where d- and hybridized p-states are found to exist for only GMax positions.

Acknowledgments

The authors would like to thank the Ohio Supercomputer Center (OSC) and the National Science Foundation (NSF), through Grant CNS 0855134, for providing computing resources. We thank Dr. Richard Irving for help with machine management. We thank the Wright Center for PVIC of the State of Ohio and the University of Toledo as well as the NSF (Grants: CMMI 1234777, CMMI 0928440, CMMI 0933069) for funding this work.

References

- Birkmire, R.W., McCandless, B.E., Hegedus, S.S., 1992. Effects of processing on CdTe/CdS materials and devices. *Int. J. Solar Energy* 12, 145–154.
- Bonnet, D., 1992. The CdTe thin film solar cell – an overview. *Int. J. Solar Energy* 12, 1–14.

- Britt, J., Ferekides, C., 1993. Thin-film CdS/CdTe solar cell with 15.8% efficiency. *Appl. Phys. Lett.* 62, 2851–2852.
- Clemminck, I., Burgelman, M., Casteleyn, M., Depuydt, B.E.N., 1992. Screen printed and sintered CdTe–CdS solar cells. *Int. J. Solar Energy* 12, 67–78.
- Compaan, A.D., Tabor, C.N., Yuxin, L., Zhirong, F., Fischer, A., 1993. CdS/CdTe solar cells by RF sputtering and by laser physical vapor deposition. In: *Photovoltaic Specialists Conference. Conference Record of the Twenty Third IEEE*, pp. 394–399.
- Dobson, K.D., Visoly-Fisher, I., Hodes, G., Cahen, D., 2000. Stability of CdTe/CdS thin-film solar cells. *Sol. Energy Mater. Sol. Cells* 62, 295–325.
- Durose, K., Edwards, P.R., Halliday, D.P., 1999. Materials aspects of CdTe/CdS solar cells. *J. Cryst. Growth* 197, 733–742.
- Dzhafarov, T.D., Yesilkaya, S.S., Yilmaz Canli, N., Caliskan, M., 2005. Diffusion and influence of Cu on properties of CdTe thin films and CdTe/CdS cells. *Sol. Energy Mater. Sol. Cells* 85, 371–383.
- Gessert, T.A., Asher, S., Johnston, S., Young, M., Dipppo, P., Corwine, C., 2007. Analysis of CdS/CdTe devices incorporating a ZnTe:Cu/Ti Contact. *Thin Solid Films* 515, 6103–6106.
- Ghandhi, S.K., Taskar, N.R., Bhat, I.B., 1987. Arsenic-doped p-CdTe layers grown by organometallic vapor phase epitaxy. *Appl. Phys. Lett.* 50, 900–902.
- Green, M.A., Emery, K., Hishikawa, Y., Warta, W., Dunlop, E.D., 2013. Solar cell efficiency tables (version 42). *Prog. Photovolt: Res. Appl.* 21, 827–837.
- Hohenberg, P., Kohn, W., 1964. Inhomogeneous electron gas. *Phys. Rev.* 136, B864.
- Jones, E.D., Stewart, N.M., Mullin, J.B., 1992. The diffusion of copper in cadmium telluride. *J. Cryst. Growth* 117, 244–248.
- Kohn, W., Sham, L.J., 1965. Self-consistent equations including exchange and correlation effects. *Phys. Rev.* 140, A1133–A1138.
- Kresse, G., 1993. Technische Universität Wien.
- Kresse, G., Furthmüller, J., 1996a. Efficient iterative schemes for ab initio total-energy calculations using a plane-wave basis set. *Phys. Rev. B* 54, 11169.
- Kresse, G., Furthmüller, J., 1996b. Efficiency of ab-initio total energy calculations for metals and semiconductors using a plane-wave basis set. *Comput. Mater. Sci.* 6, 15–50.
- Kresse, G., Hafner, J., 1993. Abinitio molecular-dynamics for liquid-metals. *Phys. Rev. B* 47, 558–561.
- Kresse, G., Hafner, J., 1994. Norm-conserving and ultrasoft pseudopotentials for first-row and transition elements. *J. Phys.: Condens. Matter* 6, 8245–8257.
- Lyubomirsky, I., Rabinal, M.K., Cahen, D., 1997. Room-temperature detection of mobile impurities in compound semiconductors by transient ion drift. *J. Appl. Phys.* 81, 6684–6691.
- Ma, J., Wei, S.-H., 2013. Origin of novel diffusions of Cu and Ag in semiconductors: the case of CdTe. *Phys. Rev. Lett.* 110, 235901.
- Madelung, O., 2004. *Semiconductors: Data Handbook*. Springer Verlag.
- Major, J.D., Proskuryakov, Y.Y., Durose, K., 2013. Impact of CdTe surface composition on doping and device performance in close Space sublimation deposited CdTe solar cells. *Prog. Photovolt: Res. Appl.* 21, 436–443.
- McCandless, B.E., Sites, J.R., 2011. Cadmium telluride solar cells. *Handbook of Photovoltaic Science and Engineering*. John Wiley & Sons, Ltd., pp. 600–641.
- Mills, G., Jónsson, H., 1994. Quantum and thermal effects in H₂ dissociative adsorption: evaluation of free energy barriers in multidimensional quantum systems. *Phys. Rev. Lett.* 72, 1124–1127.
- Monkhorst, H.J., Pack, J.D., 1976. Special points for Brillouin-zone integrations. *Phys. Rev. B* 13, 5188.
- Perdew, J.P., Zunger, A., 1981. Self-interaction correction to density-functional approximations for many-electron systems. *Phys. Rev. B* 23, 5048–5079.
- Roehl, J.L., Kolagatla, A., Ganguri, V.K.K., Khare, S.V., Phaneuf, R.J., 2010. Binding sites and diffusion barriers of a Ga adatom on the GaAs(001)-c(4 × 4) surface from first-principles computations. *Phys. Rev. B* 82, 165335.
- Roehl, J.L., Aravelli, S., Khare, S.V., Phaneuf, R.J., 2012. Diffusion of a Ga adatom on the GaAs(001)-c(4 × 4)-heterodimer surface: a first principles study. *Surf. Sci.* 606, 1303–1307.
- Rohatgi, A., 1992. A study of efficiency limiting defects in polycrystalline CdTe/CdS solar cells. *Int. J. Solar Energy* 12, 37–49.
- Soo, Y.L., Huang, S., Kao, Y.H., Compaan, A.D., 1999. Annealing effects and Te mixing in CdTe/CdS heterojunctions. *Appl. Phys. Lett.* 74, 218–220.
- Vanderbilt, D., 1990. Soft self-consistent pseudopotentials in a generalized eigenvalue formalism. *Phys. Rev. B* 41, 7892–7895.
- Wei, S.-H., Zhang, S., 2002. Chemical trends of defect formation and doping limit in II–VI semiconductors: the case of CdTe. *Phys. Rev. B* 66, 155211.
- Wolf, H., Wagner, F., Kronenberg, J., Wichert, T., Grill, R., Belas, E., 2008. ISOLDE collaboration, drift-diffusion of highly mobile dopants in CdTe. *Diffus. Fundam.* 8, 3.1–3.8.